JOURNAL OF GEOPHYSICAL RESEARCH, VOL. 105, NO. B12, PAGES 28,211–28,222, DECEMBER 10, 2000

Topographic phase recovery from stacked ERS interferometry and a low-resolution digital elevation model

David T. Sandwell and Lydie Sichoix

Scripps Institution of Oceanography, La Jolla, California

Abstract. A hybrid approach to topographic recovery from ERS interferometry is developed and assessed. Tropospheric/ionospheric artifacts, imprecise orbital information, and layover are key issues in recovering topography and surface deformation from repeat-pass interferometry. Previously, we developed a phase gradient approach to stacking interferograms to reduce these errors and also to reduce the short-wavelength phase noise (see *Sandwell and Price* [1998] and Appendix A). Here the method is extended to use a low-resolution digital elevation model to constrain long-wavelength phase errors and an iteration scheme to minimize errors in the computation of phase gradient. We demonstrate the topographic phase recovery on 16-m postings using 25 ERS synthetic aperture radar images from an area of southern California containing 2700 m of relief. On the basis of a comparison with 81 GPS monuments, the ERS-derived topography has a typical absolute accuracy of better than 10 m except in areas of layover. The resulting topographic phase enables accurate two-pass, real-time interferometry even in mountainous areas where traditional phase unwrapping schemes fail. As an example, we form a topography-free (127-m perpendicular baseline) interferogram spanning 7.5 years; fringes from two major earthquakes and aseismic slip on the San Andreas Fault are clearly isolated.

1. Introduction

Phase derived from repeat-pass radar interferometry [*Gabriel et al.*, 1989; *Massonnet and Feigl*, 1998] contains at least seven contributions of varying magnitude, characteristic length scale, a priori knowledge, and scientific importance (Table1). Many research studies focus on the isolation and interpretation of an individual component such as the atmospheric delay due to water vapor, the surface deformation due to volcanic inflation, or the topography of the Earth. However, as the signal of interest approaches a single interferometric fringe, accurate removal of the unwanted components becomes more challenging. Our long-term objective is to understand the mechanisms by which the Earth deforms throughout an earthquake cycle. Coseismic and even postseismic deformations have been observed for moderate and large earthquakes by many investigators [*Massonnet et al.*, 1993; *Peltzer et al.*, 1996] because the line-of-sight signals generally exceed one interferometric fringe (i.e., 28 mm for ERS interferometry). However, attempts to observe the smaller-amplitude interseismic strains are sometimes confused by contributions from the unmodeled signals. In these cases, a common approach is to visually examine numerous interferograms which presumably have differing time-dependent error sources (i.e., ionosphere, troposphere, and phase noise) to gain confidence in the interpretation of the small surface changes. However, when the baseline length is $\gtrsim$100 m, phase due to unmodeled topography or phase unwrapping errors creep into the solutions adding further uncertainty to the interpretation. In this paper we present an approach, or recipe, for isolating the topographic phase in cases where many repeat synthetic aperture radar (SAR) images are available.

The approach does not contain significant new ideas or new mathematical formulations, but it is the combination of a variety of published methods. Increasing the interferometric baseline increases the sensitivity to topography but at the expense of reducing the correlation. For C band, ERS interferometry in mountainous areas, there is an optimal baseline length of ~100-200 m [*Li and Goldstein*, 1990; *Madsen et al.*, 1993; *Zebker et al.*, 1994a]. Phase noise can be reduced by complex multilooking [*Li and Goldstein*, 1990] and also by using filters with smaller sidelobes than a boxcar [*Lee et al.*, 1998; *Sandwell and Price*; 1998]. However, in areas of rugged terrain the filter length must be shorter than the length scale of the residual topographic phase. *Massonnet and Feigl* [1998] note the importance of removal of as much known phase as possible prior to the complex multilook operation. *Ghiglia and Pritt* [1998] discuss the various approaches to two-dimensional phase unwrapping and, in particular, note the importance of masking areas of layover. *Poehler et al.* [1998] provide a remove/restore recipe for automatic digital elevation model (DEM) generation. *Hanssen and Klees* [1999] assess DEM accuracy degradation due to vertical atmospheric stratification. This final issue is particularly important in our area because of the large relief (2700 m) coupled with the wide seasonal temperature and water vapor variations.

2. Recipe for Topography

Our approach is based on the classic remove/restore procedure combined with stacking [*Sandwell and Smith*, 1997]. The objective is to develop a topographic phase that is precisely aligned to the radar coordinate system and has sufficient resolution and accuracy to remove all topographic effects from any interferogram in the stack.

1. Select a master single-look-complex (SLC) image and associated master orbit and geolocate one reflector in the image.

Paper number 2000JB900340.
0148-0227/00/2000JB900340$09.00

Table 1. Contributions to Interferometric Phase

Phase Component	Length Scale	Knowledge to Remove	Scientific Importance
Earth curvature[a]	ellipsoid (WGS84)	known	—
Topographic phase[b]	broad spectrum	known at long λ	foundation for all fields[c]
Surface deformation[d]	broad spectrum	unknown	geology, geophysics, glaciology, etc.[e]
Orbit error[f]	almost a plane	unknown	—
Ionospheric delay[g]	red spectrum	long λ known from GPS	ionospheric scientists
Tropospheric delay[h]	power law	unknown	atmospheric scientists
Phase noise[i]	white spectrum	unknown	—

[a] *Joughin et al.* [1996].
[b] *Zebker and Goldstein* [1986], *Zebker et al.* [1994a], and *Jakowatz et al.* [1996].
[c] *Evans et al.* [1995], and *Burke and Dixon* [1988].
[d] *Massonnet et al.* [1993], *Zebker et al.* [1994b], and *Peltzer et al.* [1996].
[e] *Massonnet and Feigl* [1998], and *Dixon et al.* [1995].
[f] *Massonnet and Rabaute* [1993].
[g] *Curlander and McDonough* [1991].
[h] *Rosen et al.* [1996], and *Hanssen et al.* [1999].
[i] *Li and Goldstein* [1990].

Both the horizontal and vertical position of the reflector should be known more accurately than the pixel resolution (<4 m for ERS). Moreover, the absolute orbit accuracy $\lesssim$0.5 m [*Scharroo and Visser*, 1998]. Figure 1 is a schematic illustration of a time history (stack) of SAR images. This represents a three-dimensional array of raw phase data containing many combinations of interferometric pairs that can be averaged and differenced.

2. Project a low-resolution digital elevation (DEM) model into the radar coordinates of the master image. The DEM is first converted from height above sea level to height above the WGS84 ellipsoid using the best available geoid height model (e.g., EGM86 [*Lemoine et al.*, 1998]). The projection from latitude, longitude, height space into range, azimuth, and phase/baseline space is accomplished by calculating both the range of closest approach and time of closest approach (azimuth) between the precise orbit trajectory and each pixel in the master image. The nonlinear transformation from height to phase-per-baseline and vice versa is based on the known orbital and ellipsoidal geometry [*Sandwell and Price,* 1998]. The known position of the reflector provides a uniform range/azimuth translation that is applied to the entire image. For ERS the range translation is -40 m for this track in California, while the azimuth translation is much larger and depends on the common doppler centroid frequency selected for the stack (e.g., 772 m).

3. Align the suite of SLC slave images to the master image. Figure 2 illustrates the important parameters in the image alignment and interferogram formation process. The first step is to identify potential interferometric pairs based on perpendicular baseline and time separation. Those pairs having short time separation (e.g., not more than the 35-day revisit time of ERS) and moderate perpendicular baselines (50-300 m) are candidates for topographic recovery (thick shaded lines in Figure 2), while pairs having longer time separation and baselines <150 are the best candidates for change detection (medium shaded lines in Figure 2). One of the images from each candidate pair is geometrically correlated with the master and then the raw SAR data are refocused to match the master image; we call this a primary match. In many cases, the interferometric correlation between the master and slave will be poor, but the important consideration is that the alignment is better than the posting spacing of the final topographic phase (i.e., 16 m by 16 m). The remaining slave images are then geometrically matched to their optimal interferometric mate; we call this a secondary match. The resulting stack contains many candidate interferometric pairs all aligned to a common topographic phase.

4. Remove the phase of the crude DEM from each slave while forming interferograms. As we show next, even a small amount of phase noise prevents accurate phase gradient estimation in areas of high topographic phase gradient (>1 rad/pixel). Thus it is essential to remove all known topographic phase from each interferogram prior to computing the phase gradient; in mountainous areas, iteration of this approach is required. To illustrate this problem, as well as the pitfalls of the first difference

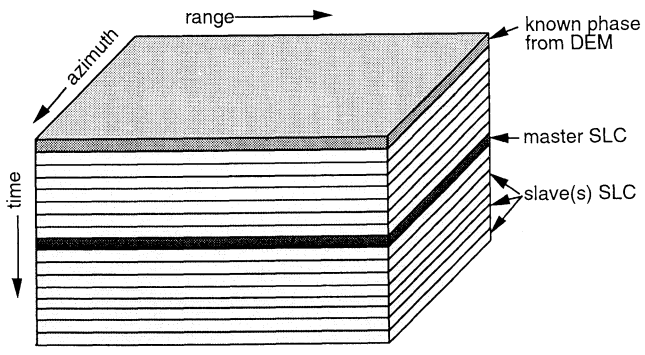

Figure 1. Diagram illustrating a stack of single-look-complex (SLC) SAR images used for both topographic recovery and change detection. The stack has three dimensions, range, azimuth, and time. Slave images are aligned to subpixel accuracy to the master image so that an interferogram can be formed from any pair in the stack, although not every pair will be coherent. The best available digital elevation model is projected into range azimuth space and converted to phase per unit baseline.

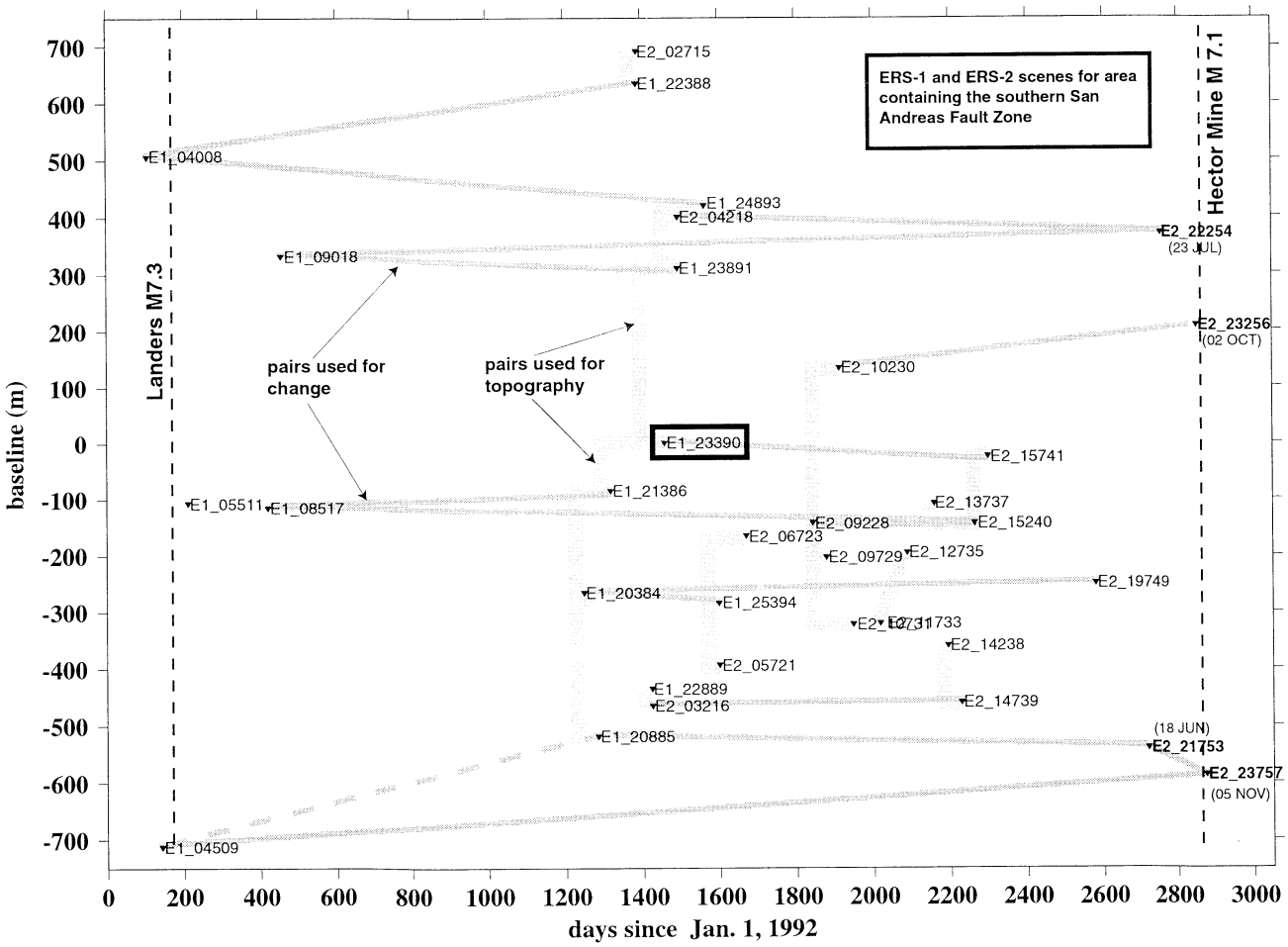

Figure 2. Diagram of available ERS-1 and ERS-2 SAR images for a 120 km by 120 km area containing the southern San Andreas Fault and the Salton Sea. Images after May 1999 were received at the Scripps Institution of Oceanography X-band receiving station. These 35 scenes span 7.5 years and include the crustal deformations of the Landers and Hector Mine earthquakes. All slave images were aligned with the master image (E1_23390). The vertical axis is the perpendicular baseline distance between the trajectory of each slave and the trajectory of the master. Phase gradients from pairs with medium baseline difference (50-300 m) and short time difference (<70 days) are stacked to construct a reference topographic phase (thick shaded lines). Pairs with short baseline difference (<150 m) and long time span are used for monitoring crustal deformation once the reference phase is removed.

operator, consider the recovery of phase gradient for a constant phase ramp as shown in Figures 3. The upper two plots show an example phase ramp of 1 rad/pixel and the sampled real and imaginary components of the interferogram. Assuming there is no noise, one can attempt to recover the phase gradient using a first-difference measurement or an optimally designed, Parks-McClellan differentiator [*Sandwell and Price,* 1998]. We have performed this experiment for phase gradients ranging from 0 to π rad/pixel to illustrate how both differentiators underestimate the true gradient. Gradients above $\pi/2$ rad/pixel cannot be accurately recovered by either method. Moreover, the first-difference operator begins to fail at about 0.5 rad/pixel. For a 200-m perpendicular baseline, this corresponds to a gradient of 4 m per 16-m pixel or a slope of 14°. On the basis of this simulation and other simulations where noise is included, we use the Parks-McClellan difference operator and edit phase gradient estimates >1 rad/pixel. Unfortunately, this editing scheme will also keep the very highest gradients (>2 rad/pixel) and record them as low values (Figure 3). As discussed below (step 7), several iterations are required to remove high phase gradient prior to interferogram formation.

5. Stack the residual and edited phase gradient following the weighting scheme of equation (A5). In addition to editing on phase gradient, we also edit data where the correlation falls below 0.3 which corresponds to a signal to noise ratio of 0.65 [*Bendat and Piersol,* 1986, p. 178]. The stacking involves two summations. The numerator of equation (A5) is the straight sum of the phase gradient with the sign modified by the sign of the perpendicular baseline. The denominator is the cumulative baseline. For the set of 17 interferograms shown in Figure 2, the maximum cumulative baseline is ~1300 m. Areas of very poor correlation or layover have cumulative baseline <400 m. Later during the phase unwrapping step, we provide zero weight in these regions [*Ghiglia and Pritt,* 1998]. Indeed, because so many interferograms are included in the stack, this on/off weighting by cumulative baseline is a robust and critical part of the recipe.

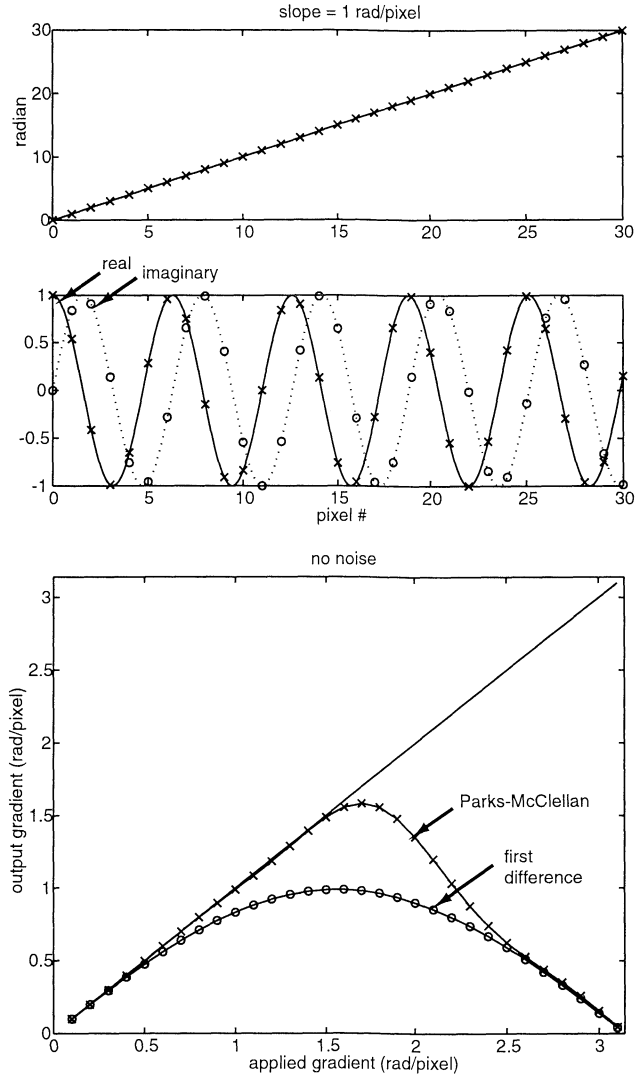

Figure 3. (top) Uniform phase gradient of 1 rad/pixel. (middle) Real and imaginary components of interferogram for uniform phase gradient are sampled once per pixel. (bottom) Estimated phase gradient (vertical axis) versus applied phase gradient (horizontal axis) for exact recovery (solid line), the first difference operator (open circles), and the Parks-McClellan [*Krauss et al.,* 1994] difference operator (crosses). No differential operators can recover phase gradient larger than $\pi/2$ rad/pixel. When 5% phase noise is present, phase gradients >1 rad/pixel are not well recovered by any method (not shown).

6. The phase is unwrapped using the Fourier cosine transform approach described in Appendix A. Initially, the unwrapping scheme takes the two gradient arrays with zeros placed in areas of low cumulative baseline (voids). Unfortunately, this initial guess of zero is rather poor because the voids are systematically on the sides of the mountains facing the radar (i.e., layover areas) where the phase gradient should be large. To prevent this systematic effect from corrupting the long-wavelength part of the phase, a high-pass filter is applied to the residual unwrapped phase (~10 km cutoff wavelength). The high-pass filtered phase provides a new estimate of phase gradient which is used only to replace the values in the void areas. After about 10 iterations, the scheme converges to a field that matches the known phase gradient and has no long-wavelength components. The assumption here is that the long wavelengths, provided by the crude DEM, are accurate and there is no crustal motion between the times of the reference and repeat passes. During the final iteration, unwrapped residual phase is output. Again, the importance of accurately masking the areas of layover cannot be overemphasized [*Ghiglia and Pritt,* 1998].

7. The unwrapped residual phase is added to the phase from the crude DEM. This provides a starting phase model for the next iteration (step 4). After about 3 iterations on 17 interferograms, this, CPU-intensive, scheme reduces the residual phase in the component interferograms to what we believe is the residual error due to atmospheric delay and orbit error. Moreover, several iterations are required to reduce the residual phase gradient to <1 rad/pixel where the numerical derivative is accurate (Figure 3). In fact, a visual inspection of the residual interferograms revealed significant atmospheric artifacts in 7 of the 17 interferograms; these 7 were eliminated from the stack for iterations 2 and 3. An example of the sequential phase removal from a component interferogram is provided in Figure 4. The initial interferogram (iteration 0) has more than 24 tightly packed fringes spanning the 2700 m elevation change from the Salton Sea to Toro Peak. Removal of the U.S. Geological Survey (USGS) 90-m DEM (phase-DEM) eliminates most of the long-wavelength topographic phase but not the small-scale features (iteration 1). Moreover, some rather large-scale topographic errors are apparent. (Note, given precise orbital information [*Scharroo and Visser,* 1998], no flattening of the interferograms is needed.) The final residual phase (iteration 4) has less than one fringe of residual phase. Some of this residual is correlated with large elevation changes but as we show in section 3, the residual topographic errors are much too small to explain these fringes; we believe they represent changes in the vertical stratification of the atmosphere [*Hanssen and Klees,* 1999].

3. Resolution and Accuracy

The final topographic phase, converted into height above the WGS84 ellipsoid, is shown in Figure 5. No attempt was made to project the grid from the radar coordinates of the master image into a geographic coordinate system since our main objective is to remove this topographic phase from candidate change detection interferograms. If the height data were projected, however, there would be gaps in the areas of layover. Known locations and heights of 81 GPS monuments are used to evaluate the height accuracy of both the USGS DEM and the new hybrid DEM (gray dots in Figure 5). One of these points on the eastern side of the Salton Sea, along the California Aqueduct, was used to translate the master image into an absolute WGS84 coordinate system. Several other prominent GPS locations were checked to be sure that the horizontal registration is accurate throughout the image. For the vertical accuracy test we eliminated points in layover areas as well as points near the edge of the frame because of Fourier edge effects of the phase unwrapping. The median absolute deviation (MAD) between the USGS DEM and the GPS heights is 12.7 m, while the hybrid DEM has a MAD of 9.7 m (Figure 6). While this is a significant improvement in accuracy, the main improvement is in terms of resolution. The USGS DEM has cells with dimensions of 90 m by 90 m, while the new hybrid DEM has cells of 16 m in azimuth by ~41 m in ground range (16 m in slant range). Since we use the USGS DEM only to control the long wavelengths (>5 km), even a 1-km resolution DEM such as GTOPO30 can be used, although more iterations are required.

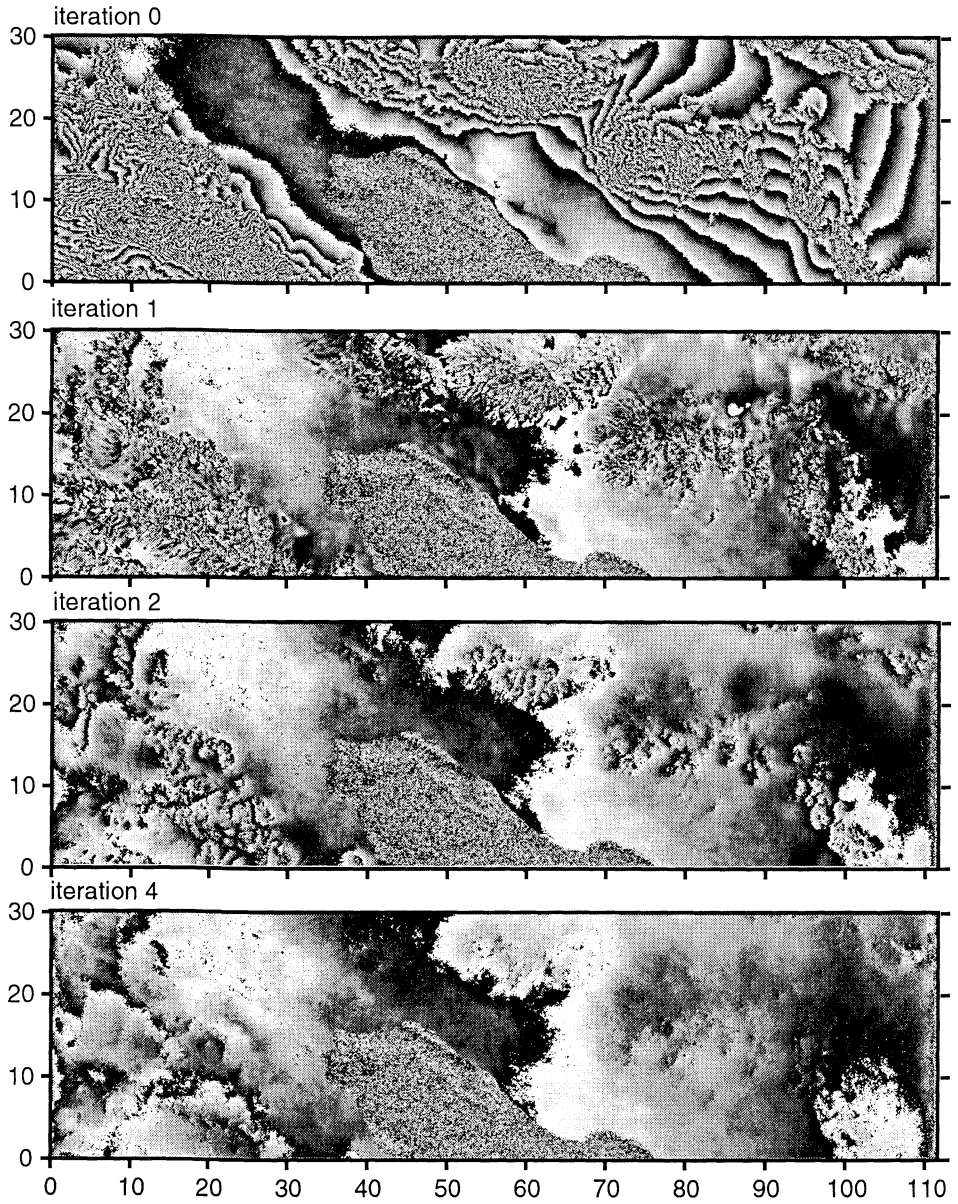

Figure 4. Sequential estimation of topographic phase. Total phase (iteration 0) of an ERS-Tandem interferogram (E2_04281 minus E1_23891) with a 90-m perpendicular baseline displays 25 fringes between the Salton Sea (-100 m) and Toro Peak (2600 m). Residual phase of interferogram (iteration 1) after removal USGS DEM (90-m postings). In addition to the small-scale phase not resolved by the 90-m DEM, there are large-scale errors in the upper right of the image. Unwrapped stacked phase gradient (iteration 2) is removed from iteration 1. Note the small-scale residuals are reduced and the large-scale residuals are gone. Final residual phase (iteration 4) reveals residual orbit error and atmospheric delay.

An example of the features resolvable in this hybrid DEM is provided in Figure 7, which corresponds to the white box in Figure 5. This area of Eagle Mountain, California, contains large settling ponds constructed on the gently sloping terrain. Features 50 m across and 10 m tall are easily resolved in the topography. This improved resolution is very important for the complete removal of topographic phase from change interferograms.

We performed a similar hybrid topographic recovery using 13 ERS SAR images for an area to the east of our study area which contains 3400 m of relief from Palm Springs to San Jacinto Peak. The higher elevations in this area are covered by snow in the wintertime and there is also tree cover. These factors reduce the interferometric correlation with respect to the Salton Sea area (Figure 5). Nevertheless, the median absolute height difference with respect to 127 GPS monuments improves to 12.4 m from 17.8 m for the USGS 90-m DEM. When 25 SAR images become available for stacking, the height accuracy will be further improved to ~10 m. Since these areas around San Jacinto Peak and Toro Peaks represent some of the most rugged terrain in western North America, we believe the ERS-derived, hybrid DEMs are suitable for two-pass change detection using typical ERS data. Our plan is to construct a high-resolution topographic

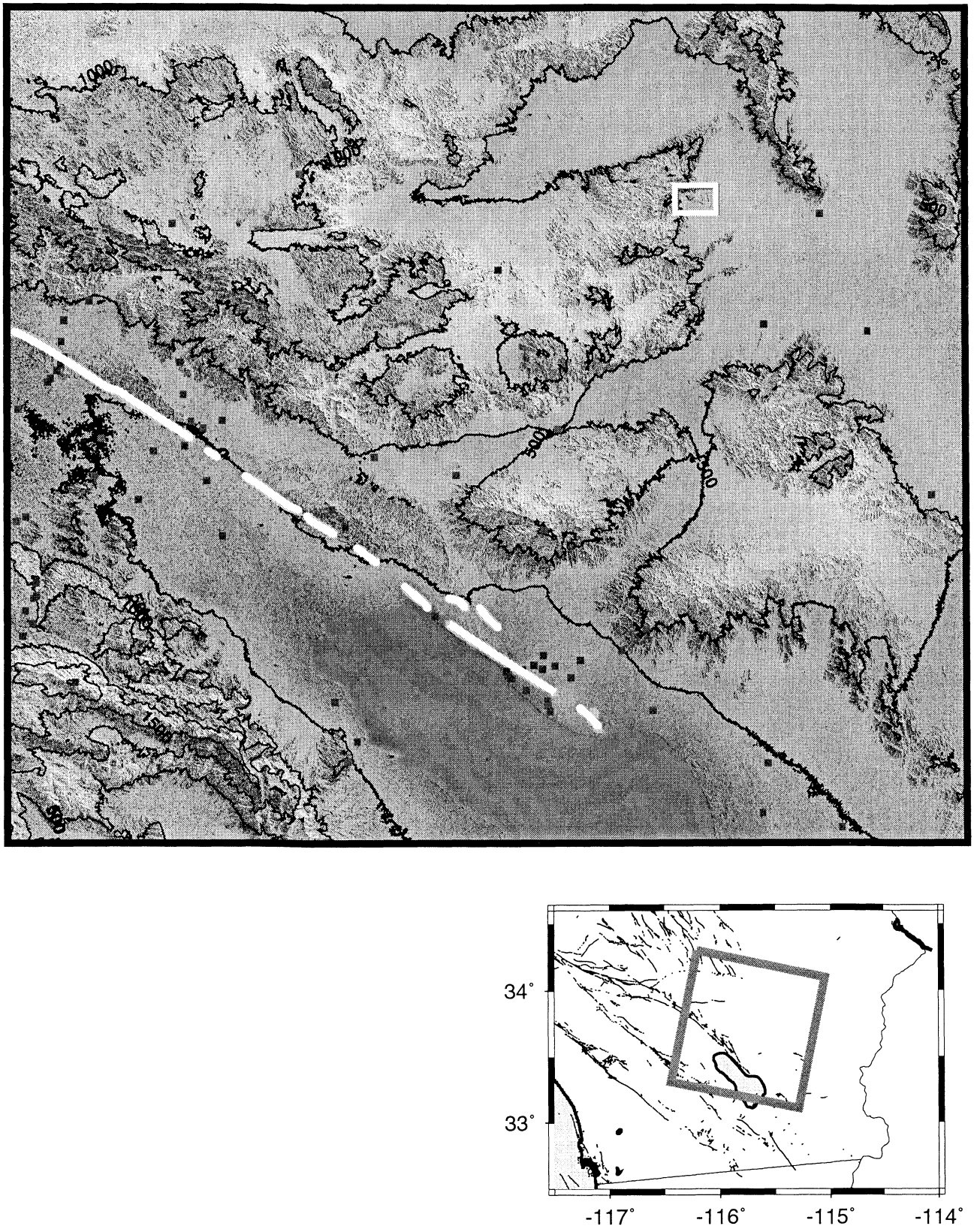

Figure 5. Topography (meters above WGS84 ellipsoid, 500 m contour interval) of Salton Sea area (see inset location map) includes the southern segment of the San Andreas Fault (white) and GPS monuments (gray). The white box contains Eagle Mountain, California (Figure 7). This topography combines the long-wavelength accuracy of the USGS 90-m DEM (referenced to the EGM96 geoid) with the short-wavelength (<6 km) phase gradient information from the stack of 25 ERS SAR images. The combined DEM has 16-m postings in range (41-m ground range),16-m postings in azimuth, and an absolute vertical accuracy of ~10 m (see Figure 6).

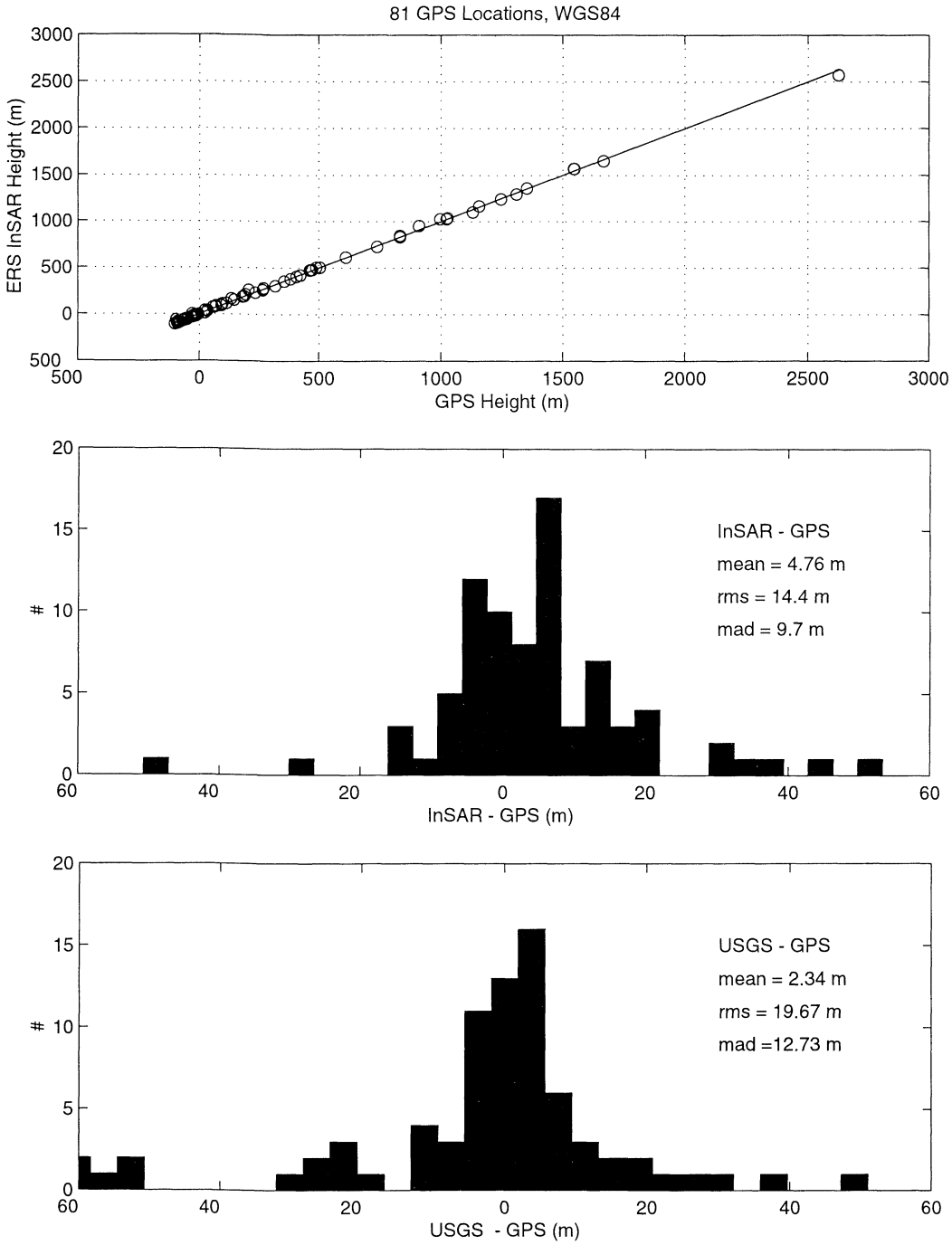

Figure 6. Comparison between ERS-derived elevation and known elevations at 81 GPS monuments. (top) The area has an overall relief of 2700 m and, for example, the ERS-derived elevation of Toro peak is 51 m lower than the GPS elevation (2624 m). (middle) Histogram of ERS height minus GPS height has a mean offset of 4.7 m and a median absolute deviation of 9.7 m. (bottom) Histogram of ERS height minus GPS height has a mean offset of 2.3 m and a median absolute deviation of 12.7 m. (Note the USGS comparison is not accurate because the topography data were projected and smoothed which reduces their accuracy and resolution somewhat.)

phase map for every frame in the southern California area and compare this with the topography data that were recently collected by the successful Shuttle Radar Topography Mission (SRTM). The SRTM mission will provide a DEM having a horizontal resolution of 30 m and a vertical accuracy of better than 15 m [*Farr et al.*, 2000]. Thus when SRTM data become available, our approach for topographic recovery will be unnecessary.

4. Change Detection

Because all of the SLC images in the stack are geometrically aligned, this topographic phase can be removed from any interferometric pair. Our approach is to interpolate the topographic phase to the full resolution of the SLC image and to apply the topographic phase correction while forming the interferogram; the baseline scale factor is adjusted continuously

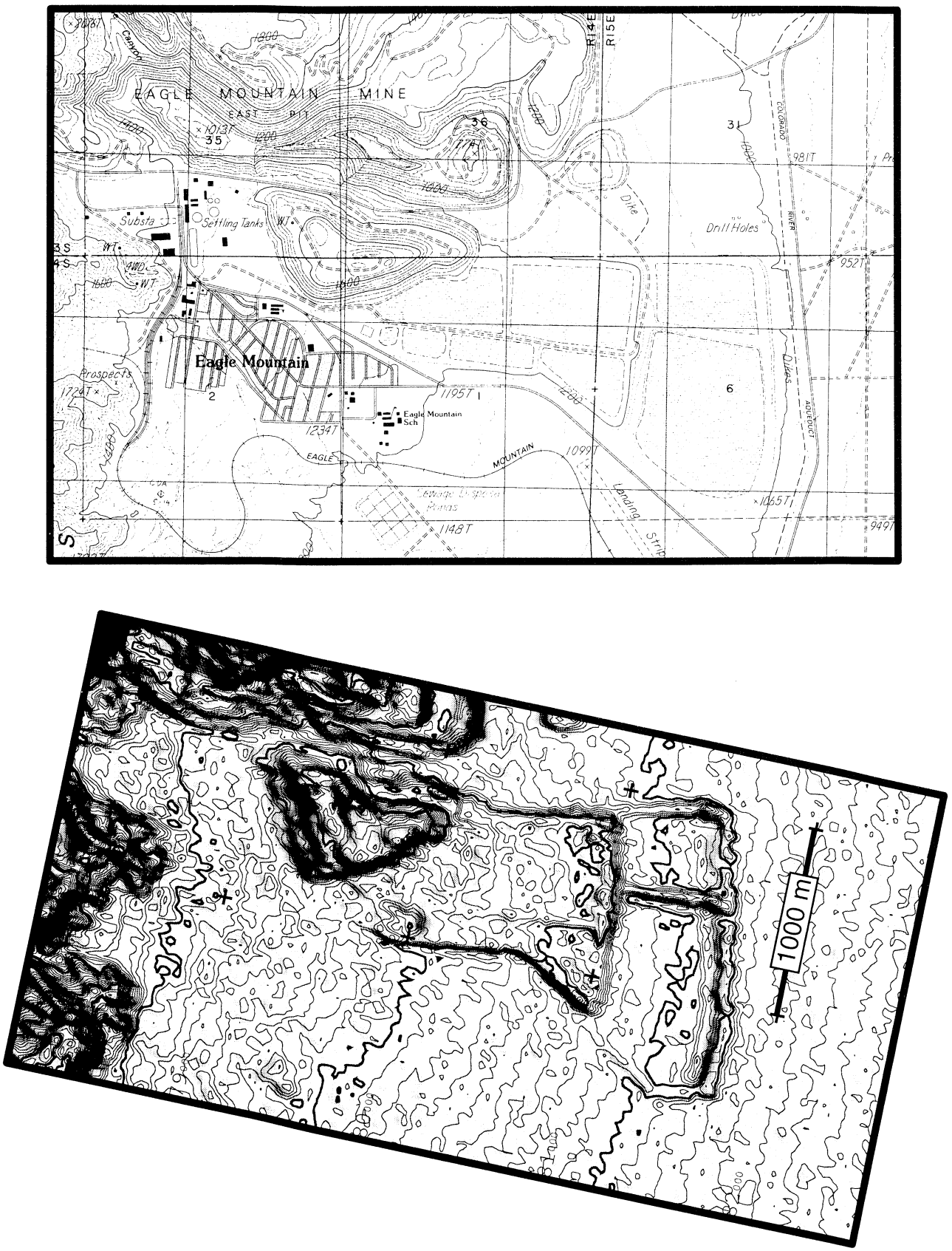

Figure 7. (top) USGS 40-foot (12.3 m) contours of Eagle Mountain Mine and the associated settling ponds. Note detailed contours for the dikes are not provided on the USGS map. (lower) DEM derived from the hybrid approach using stacked ERS-interferometry to constrain short wavelength variations (5-m contour interval). Note the eastern-most dikes were formed from the material excavated on the inboard side. The wavelength of this signature is less than 200 m and features as small as 50 m are resolved.

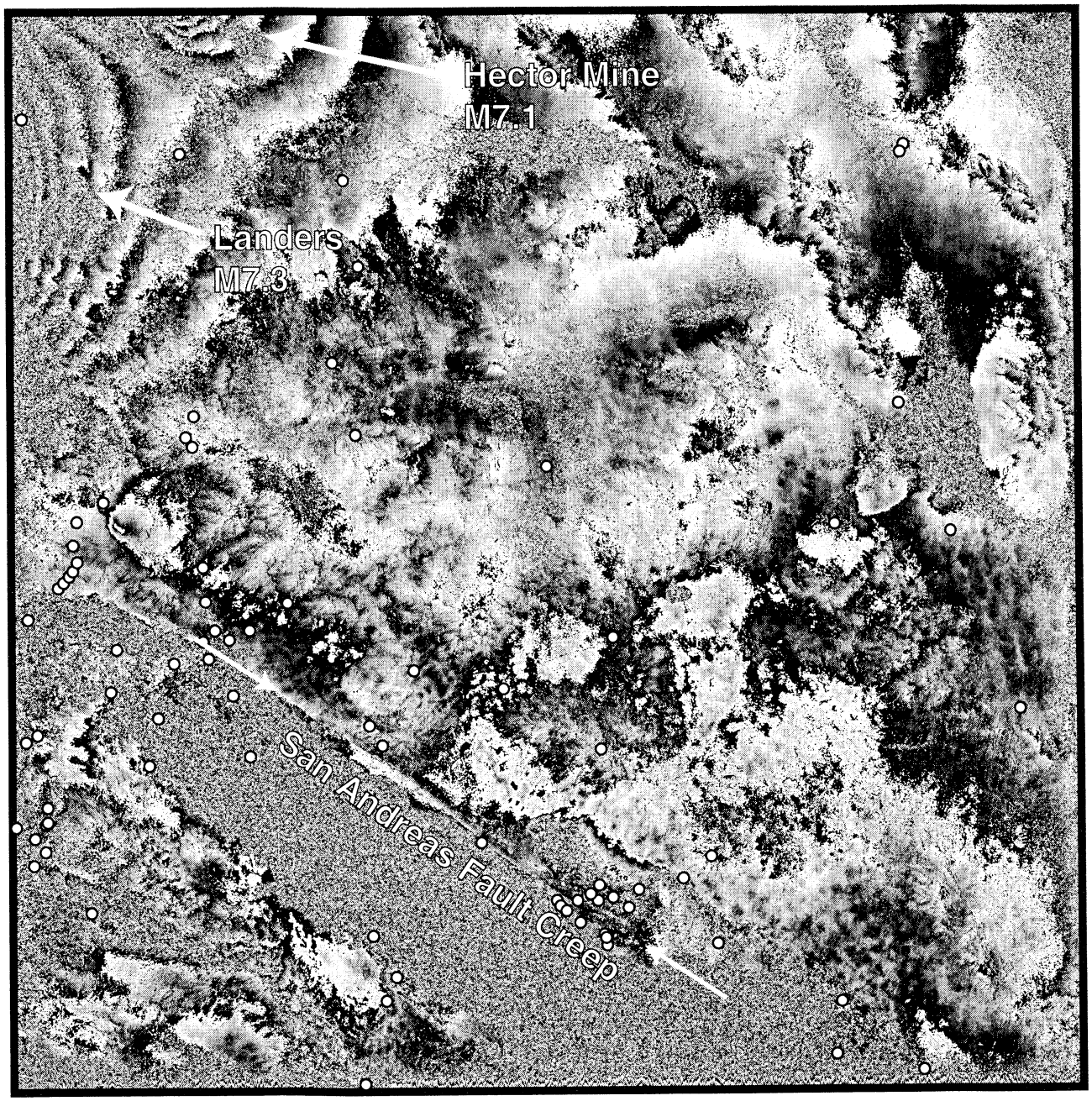

Figure 8. Interferogram with 125-m perpendicular baseline and 7.5-year time span includes deformation signals from both the Landers and Hector Mine earthquakes (E1_04509 to E2_23757 in Figure 2). Significant slip on the San Andreas Fault occurs during these two events as well as during the intervening period (between white arrows). White dots are the locations of 81 GPS monuments. This interferogram has three remarkable attributes: (1) it spans 7.5 years with adequate correlation in non vegetated areas; (2) despite the long baseline, the fringes due to topography and earth curvature are removed accurately with no orbital adjustment or flattening; and (3) the repeat pass was collected at the SIO ground station on November 5, 1999, and the interferogram was ready the following day.

in both range and azimuth to reflect the changing geometry. This early removal of the topographic phase has the effect of increasing the correlation estimate because all pixels, within the correlation window, have nearly the same phase [*Lee et al.*, 1998]. Moreover, interferograms with poor correlation can be filtered (i.e., complex multilook) over a larger area to help suppress the short-wavelength noise. As an example, we formed an interferogram with a 7.5-year time interval and a 127-m perpendicular baseline (Figure 8). For this baseline, there would normally be 34 fringes between the Salton Sea (-100 m) and Toro Peak (2600 m), while after removal, only two fringes remain. These two fringes may represent actual tectonic deformation over this interval since we expect to see 75 mm of line-of-sight deformation due to right-lateral strain across the fault zone. The more interesting aspect of this interferogram is that it spans both the Landers 1992 earthquake (M_w 7.3) and the Hector Mine

earthquake (M_w 7.2), and fringes from both are apparent in the upper left corner. Even more interesting is the 20 mm of creep that has occurred along the San Andreas Fault (marked by arrows in Figure 8). The width of this fault creep signature provides an estimate of the depth to the locked portion of the fault of ~800 m. There are 12 other candidate change detection interferograms all showing the broad strain across the fault as well as varying amount of fault creep. We are in the process of examining these tectonic deformations in greater detail.

Appendix A

A1. Stacking Phase Gradient

The phase gradient can be computed directly from the real and imaginary components of the interferogram [*Werner et al.*, 1992; *Price and Sandwell*, 1998; *Sandwell and Price*, 1998] without first computing the phase. Moreover, phase gradients can be averaged or differenced to recover topographic gradient or surface strain without phase unwrapping. The average of the phase gradient from many repeat interferograms, having different baselines, will eventually fill gaps due to temporal and baseline decorrelation. A long-term average should also minimize the phase errors due to tropospheric and ionospheric delay and thus provide an accurate topographic model for change detection interferograms [*Zebker et al.*, 1997; *Fujiwara et al.*, 1998].

Assume there is no ground displacement between the time of the reference and repeat orbits. Phase difference ϕ is related to the range difference $\delta\rho$ by $\phi = (-4\pi/\lambda)\delta\rho$. Using the law of cosines and the parallel ray approximation one finds [e.g., *Zebker and Goldstein*, 1986; *Rosen et al.*, 1996, 2000] the phase is

$$\phi = \frac{-4\pi}{\lambda} B \sin(\theta - \alpha). \tag{A1}$$

The derivative of the phase with respect to range is

$$\frac{\partial\phi}{\partial\rho} = \frac{-4\pi}{\lambda} B \cos(\theta - \alpha)\frac{\partial\theta}{\partial\rho}. \tag{A2}$$

The phase gradient depends on two terms, the perpendicular component of the baseline $B_\perp = B\cos(\theta-\alpha)$ and the derivative of look angle with respect to range $\partial\theta/\partial\rho$. This function $\partial\theta/\partial\rho$ is a mapping of the topography of the Earth. If it becomes negative, the topography is laid over in which case, topographic phase recovery is not possible. Since $\partial\theta/\partial\rho$ does not change with time, the phase gradient scales according to the perpendicular baseline.

The standard approach to adding or subtracting wrapped phase requires phase unwrapping, scaling the phase by the ratio of the perpendicular baseline and finally forming the average [*Zebker et al.*, 1994b]. Here we avoid phase unwrapping or delay it until the final step of the processing. Suppose ϕ_l and ϕ_s are wrapped phases of two interferograms having long (l) and short (s) baselines, respectively. Because the phase is wrapped, one cannot usually scale ϕ_s into ϕ_l (higher fringe rate) or vice versa unless the baselines are integer related [*Massonnet et al.*, 1996]. However, one can compute and scale the phase gradient. Using the chain rule, we find that the gradient of the phase $\phi = \tan^{-1}(I/R)$ is

$$\nabla\phi(\mathbf{x}) = \frac{R\nabla I - I\nabla R}{R^2 + I^2}, \tag{A3}$$

where $R(\mathbf{x})$ and $I(\mathbf{x})$ are the real and imaginary components of the interferogram. The interferogram is the product of two geometrically matched SLC images. Unlike the wrapped phase, which contains many 2π jumps, the real and imaginary components of the interferogram are continuous functions, and thus the gradient can be computed with a convolution operation (or by a fast Fourier transform). Because this is a finite difference of nearby pixels, one must minimize the overall phase gradient prior to computing the derivatives. The average phase gradient from N interferograms each having a perpendicular baseline b_i is

$$\overline{\nabla\phi} = \frac{1}{N}\sum_{i=1}^{N}\frac{1}{b_i}\nabla\phi_i, \tag{A4}$$

where $\overline{\nabla\phi}$ is the phase gradient per unit baseline. During averaging, one can weight regions of the individual interferograms according to the local correlation and local topographic gradient to achieve an optimal mix.

Proper weighting of the component interferograms will depend on many factors, however, it is clear that the simple unweighted average (equation (A4)) is not correct. Consider the average of one 10-m baseline and several 100-m baseline interferograms; the short baseline interferogram will dominate the stack, yet it could be contaminated by atmospheric artifacts. A more reasonable assumption is that each phase gradient estimate has about the same noise level, independent of baseline length. In this case, the components should be weighted by the absolute baseline length

$$\overline{\nabla\phi} = \frac{\sum_{i=1}^{N}\frac{|b_i|}{b_i}\nabla\phi_i}{\sum_{i=1}^{N}|b_i|} = \frac{\sum_{i=1}^{N}\mathrm{sgn}(b_i)\nabla\phi_i}{\sum_{i=1}^{N}|b_i|}. \tag{A5}$$

The cumulative baseline in the denominator of (A5) should be large to achieve maximum noise reduction. Longer baselines will provide better noise reduction and increased sensitivity to topography but these estimates will not be reliable in areas of rugged terrain and the longer baselines (>200 m) will have poorer correlation; hopefully, the estimates from shorter baselines will fill these gaps. Areas of layover can never be filled, and these data gaps pose a major obstacle to the phase unwrapping scheme outlined below [*Zebker and Lu*, 1997; *Ghiglia and Pritt*, 1998]. In practice, a suite of baselines will provide the best estimate of $\nabla\phi$.

A2. Unwrapping Phase Gradient

Let $\mathbf{u}(\mathbf{x}) = (\partial\phi/\partial x, \partial\phi/\partial y)$ be the numerical estimates of phase gradient (range, azimuth) as given in (A3), (A4), or (A5). Any vector field can be written as the sum of two vectors as follows:

$$\mathbf{u} = \nabla\phi + \nabla\times\psi, \tag{A6}$$

where ϕ is a scalar potential and ψ is a vector potential. We assume that the topographic phase is a conservative function so that the rotational part of the vector field must be zero everywhere. However, layover, filtering, and stacking interferograms introduce a rotational component that should be eliminated. This is accomplished by taking the divergence of

(A6) since $\nabla \bullet \nabla \times \psi \equiv 0$ The phase and phase gradient are now related by the following differential equation:

$$\nabla \bullet \mathbf{u} = \nabla^2 \phi. \tag{A7}$$

For a finite region the outward component of the phase gradient should be zero along the boundaries [*Ghiglia and Romero*, 1994] $\nabla\phi \bullet \mathbf{n} = 0$, where $\mathbf{n}$ is the outward normal. The two-dimensional Fourier transform of (A7) provides an algebraic relationship between the total phase $\phi_{tot}(\mathbf{k})$ and the measured phase gradient $\mathbf{u}$:

$$\phi_{tot}(\mathbf{k}) = \Im_2^{-1}\left[\frac{k \bullet \Im_2[\mathbf{u}]}{2\pi|\mathbf{k}|^2}\right], \tag{A8}$$

where $\mathbf{k} = (1/\lambda_x, 1/\lambda_y)$ and $\Im_2[\bullet]$ and $\Im_2^{-1}[\bullet]$ are the forward and inverse two-dimensional Fourier transform, respectively. The zero phase-gradient boundary condition is automatically satisfied if the Fourier transform has only cosine components [*Ghiglia and Romero* 1994; *Press et al.,* 1992, p. 514]. Note that this is the standard geodetic approach for computing the geoid height from the deflections of the vertical [*Heiskanen and Moritz*, 1967].

Acknowledgments. Our SAR processing software is based on the Stanford/JPL algorithms for image focussing and precise alignment provided by Howard Zebker. Much of the phase gradient and stacking was performed with the GIPS system written by Peter Ford at MIT using filters designed with the MATLAB Signal Processing Toolbox. SAR data were provided by the European Space Agency through its distributors SpotImage and Eurimage. The research was funded by NASA HPCC/ESS CAN and the National Science Foundation, Instrument and Facilities Program.

References

Bendat, J. S., and A. G. Piersol, *Random Data Analysis and Measurement Procedures*, 2nd ed., John Wiley, New York, 1986.

Burke, K., and T. H. Dixon, Topographic Science Working Group report, Land Processes Branch, Code EEL, NASA, Washington, D. C., 1988.

Curlander, J. C., and R. N. McDonough, *Synthetic Aperture Radar: Systems & Signal Processing*, edited by J.A. Kong, John Wiley, New York, 1991.

Dixon, T. H., et al., SAR interferometry and surface change detection, *Tech. Rep. TR 95-003*, Univ. of Miami, Rosenstiel Sch. of Mar. and Atmos. Sci., Miami, Fla., 1995.

Evans, D. L., et al., Spaceborne synthetic aperture radar: Current status and future directions, *NASA Tech. Memo., TM-4679*, 1995.

Farr, T. G., P. Rosen, S. Hensley, E. Rodrigues, Ja Martin and M. Kobrick, The Shuttle Radar Topography Mission, *Eos Trans. AGU, 81*(19), Spring Meet. Suppl., S163, 2000.

Fujiwara, S., P. A. Rosen, M. Tobita, and M. Murakami, Crustal deformation measurements using repeat-pass JERS 1 synthetic aperture radar interferometry near the Izu Peninsula, Japan, *J. Geophys. Res., 103*, 2411-2426, 1998.

Gabriel, A. K., R. M. Goldstein, and H. A. Zebker, Mapping small elevation changes over large areas: Differential radar interferometry, *J. Geophys. Res., 94*, 9183-9191, 1989.

Ghiglia, D. C., and M. D. Pritt, *Two-Dimensional Phase Unwrapping: Theory, Algorithms, and Software*, John Wiley, New York, 1998.

Ghiglia, D. C., and L. A. Romero, Robust two-dimensional weighted and unweighted phase unwrapping that uses fast transforms and iterative methods, *J. Opt. Soc. Am., 11*, 107-117, 1994.

Hanssen, R., and R. Klees, An empirical model for the assessment of DEM accuracy degradation due to vertical atmospheric stratification, paper presented at Second International Workshop on ERS SAR Interferometry, FRINGE'99, European Space Agency, Liege, Belgium, 1999.

Hanssen, R. F., H. A. Weckwerth, H. A. Zebker, and R. Klees, High-resolution water vapor mapping from interferometric radar measurements, *Science, 283*, 1297-1299, 1999.

Heiskanen, W. A., and H. Moritz, *Physical Geodesy*, W. H. Freeman, New York, 1967.

Jakowatz, C. V., D. E. Wahl, P. H. Eichel, D. C. Ghiglia, and P. A. Thompson, *Spotlight-Mode Synthetic Aperture Radar: A Signal Processing Approach*, Kluwer Acad., Norwell, Mass., 1996.

Joughin, I., M. Winebrenner, R. Fahnestock, R. Kwok, and W. Krabill, Measurement of ice sheet topography using satellite-radar interferometry, *J. Glaciol., 42*, 10-22, 1996.

Krauss, T. P., L. Shure, and J. N. Little, *Signal Processing TOOLBOX for Use With Matlab*, Math Works, Natick, Mass., 1994.

Lee, J. S., K. P. Papthanassiou, T. L. Ainsworth, M. R. Grunes, and A. Reigber, A new technique for noise filtering of SAR interferometric phase images, *IEEE Trans. Geosci. Remote Sens., 36*, 1456-1465, 1998.

Lemoine, F. G., et al., The development of the joint NASA GSFC and the National Imagery and Mapping Agency (NIMA) geopotential model EGM96, *NASA, TP-1998-206861*, NASA Goddard Space Flight Cent., Greenbelt, Md. , 1998.

Li, F. K., and R. M. Goldstein, Studies of multibaseline spaceborne interferometric synthetic aperture radar, *IEEE Trans. Geosci. Remote Sens., 28*, 88-97, 1990.

Madsen, S. N., H. A. Zebker, and J. martin, Topographic mapping using radar interferometry: Processing techniques, *IEEE Trans. Geosci. Remote Sens., 31*, 246-255, 1993.

Massonnet, D., and K. Feigl, Radar interferometry and its application to changes in the Earth's surface, *Rev. Geophys., 36*, 441-500, 1998.

Massonnet, D., and T. Rabaute, Radar interferometry: Limits and potential, *IEEE Trans. Geosci. Remote Sens., 31*, 455-464, 1993.

Massonnet, D., M. Rossi, C. Carmona, F. Adragna, G. Peltzer, K. Feigl, and T. Rabaute, The displacement field of the Landers earthquake mapped by radar interferometry, *Nature, 364*, 138-142, 1993.

Massonnet, D., H. Valdon, and M. Rossi, Reduction of the need for phase unwrapping in radar interferometry, *IEEE Trans. Geosci. Remote Sens., 34*, 489-497, 1996.

Peltzer, G., P. Rosen, F. Roges, and K. Hudnut, Postseismic rebound in fault step-overs caused by pore fluid, *Science, 273*, 1202-1204, 1996.

Poehler, P. L., A. W. Mansfield, N. N. Haag, and H. Rais, Photogrammetric techniques for interferometric synthetic aperture radar data exploitation, report, Sci. Appl. Int. Corp., San Diego, Calif., 1998.

Press, W. H., S. A. Teukolsky, W. T. Vetterling, and B. P. Flannery, *Numerical Recipes in C*, 2nd ed., Cambridge Univ. Press, New York, 1992.

Price, E. J., and D. T. Sandwell, Small-scale deformations associated with the 1992 Landers, California, earthquake mapped by synthetic aperture radar interferometry phase gradients, *J. Geophys. Res., 103*, 27,001-27,016, 1998.

Rosen, P. A., S. Hensley, H. A. Zebker, F. H. Webb, and E. Fielding, Surface deformation and coherence measurements of Kilauea Volcano, Hawaii from SIR-C radar interferometry, *J. Geophys. Res., 101*, 23,109-23,125, 1996.

Rosen, P. A., S. Hensley, I. R. Joughin, F. K. Li, S. N. Madsen, E. Rodrigues and R. M. Goldstein, Synthetic aperture radar interferometry, *Proc. IEEE, 88*(3), 333-382, 2000.

Sandwell, D. T., and E. J. Price, Phase gradient approach to stacking interferograms, *J. Geophys. Res., 103*, 30,183-30,204, 1998.

Sandwell, D. T., and W. H. F. Smith, Marine gravity anomaly from Geosat and ERS-1 satellite altimetry, *J. Geophys. Res., 102*, 10,039-10,054, 1997.

Scharroo, R., and P. Visser, Precise orbit determination and gravity field improvement for the ERS satellites, *J. Geophys. Res., 103*, 8113-8127, 1998.

Werner, C. L., S. Hensley, R. M. Goldstein, P.A. Rosen, and H. Zebker, Techniques and applications of SAR interferometry for ERS-1:

Topographic mapping, change detection and slope measurement, paper presented at First ERS-1 Symposium: Space at the Service of our Environment, Eur. Space Agency, Cannes, France, 1992.

Zebker, H. A., and R. M. Goldstein, Topographic mapping from interferometric synthetic aperture radar observations, *J. Geophys. Res., 91*, 4993-4999, 1986.

Zebker, H. A., and Y. Lu, Phase Unwrapping algorithms for radar interferometry: Residue-cut, least squares, and synthesis algorithms, *J. Opt. Soc. Am., 15*, 586-598, 1997.

Zebker, H. A., C. L. Werner, P. A. Rosen, and S. Hensley, Accuracy of topographic maps derived from ERS-1 interferometric radar, *IEEE Trans. Geosci. Remote Sens., 32*, 823-836, 1994a.

Zebker, H. A., P. A. Rosen, and R. M. Goldstein, On the derivation of coseismic displacement fields using differential radar interferometry: The Landers earthquake, *J. Geophys. Res., 99*, 19,617-19,634, 1994b.

Zebker, H. A., P. A. Rosen, and S. Hensley, Atmospheric effects in interferometric synthetic aperture radar surface deformation and topographic maps, *J. Geophys. Res., 102*, 7547-7563, 1997.

D.T. Sandwell and L. Sichoix, Scripps Institution of Oceanography, University of California, San Diego, IGPP 0225, 9500 Gilman Dr., La Jolla, CA 92093-0225. (dsandwell@ucsd.edu)

(Received March 8, 2000; revised August 8, 2000;
accepted September 6, 2000.)